


Insights into lattice oxygen and strains of oxide-derived copper for ammonia electrosynthesis from nitrate

Received: 22 October 2024

Accepted: 2 April 2025

Published online: 11 April 2025

 Check for updatesQinyue Wu¹, Xinfei Fan², Bing Shan³, Liang Qi¹, Xie Quan¹ & Yanming Liu^{1,4}✉

Electrocatalytic NO_3^- reduction (eNO3RR) is a sustainable method for purification of NO_3^- wastewater and NH_3 recovery. Cu-based catalysts are promising for eNO3RR, but insufficient active hydrogen ($^*\text{H}$) supply and $^*\text{NO}_2$ poison of active sites have hindered their performance, and the catalytic mechanism remains ambiguous. Here, we report oxide-derived copper nanosheet arrays (OD-Cu NSs) with residual lattice oxygen and lattice strains to enhance NH_3 synthesis from eNO3RR. It is efficient for NH_3 synthesis with high Faradaic efficiencies of 88.7–99.7% and maximum NH_3 yield of $6.20 \text{ mmol} \cdot \text{h}^{-1} \cdot \text{cm}^{-2}$ at neutral solution, 10–140 mM NO_3^- and 50–1500 $\text{mA} \cdot \text{cm}^{-2}$. Experimental and theoretical results reveal that lattice oxygen regulates the electronic structure of OD-Cu NSs and promotes $^*\text{NO}_2$ conversion, while lattice strain enhances $^*\text{H}$ generation from water dissociation, resulting in the good performance for NH_3 synthesis. The applicability of OD-Cu NSs is proved by the high recovery of ammonia compound from eNO3RR.

NH_3 is an important chemical with extensive applications in agriculture, chemical industries, and the energy sectors¹. However, NH_3 synthesis currently relies on the conventional Haber-Bosch process². It requires high temperature and pressure, which consumes about 1–2% of global energy and emits large amounts of CO_2 ³. Consequently, a green and low-energy method for NH_3 synthesis is urgently needed. Electrocatalytic NO_3^- reduction (eNO3RR) has emerged as a promising alternative for NH_3 synthesis owing to its mild operating conditions and low energy consumption ($<0.5 \text{ kWh} \cdot \text{g}_{\text{N}}^{-1}$)⁴. Moreover, eNO3RR can tackle NO_3^- pollution in water, one of the major environmental problems resulted from agricultural and industrial activities. It not only purifies water but also recovers NH_3 from NO_3^- rich wastewater.

NH_3 synthesis from eNO3RR is highly dependent on electrocatalysts. Among the various catalysts reported, Cu-based catalysts are good candidates as the high electron density of Cu d-orbital is favorable for NO_3^- adsorption and the initiation of eNO3RR⁵. However,

eNO3RR process involves complex steps, including proton-coupled electron transfer, the adsorption and hydrogenation of reactants and intermediates⁶. The eNO3RR on Cu-based catalysts is hindered by the inherent defects of $^*\text{NO}_2$ poison (intermediates for eNO3RR) and weak $^*\text{H}$ supply on Cu^{7,8}. The Cu surface has abundant free electrons. It forms strong adsorption with $^*\text{NO}_2$ through the electron coupling effect⁹, poisoning the active sites¹⁰. Moreover, the hydrogenation of intermediates is also crucial for eNO3RR. Cu is known to be inefficient for $^*\text{H}$ generation from water dissociation due to its high energy barrier¹¹. The slow $^*\text{H}$ supply limits the hydrogenation kinetics for eNO3RR. To enhance NH_3 synthesis from eNO3RR, $^*\text{NO}_2$ conversion or $^*\text{H}$ supply has been regulated by the strategies such as metal/non-metal atom doping^{7,12,13}, microstructure regulation¹⁴, design of atomically dispersed Cu^{15,16} and Cu/Cu₂O heterojunction^{17,18}. Despite the progresses have been made, simultaneous optimization of $^*\text{NO}_2$ conversion and $^*\text{H}$ supply to enhance NH_3 electrosynthesis from eNO3RR has been rarely reported. Meanwhile, tailoring active sites that are both

¹Key Laboratory of Industrial Ecology and Environmental Engineering (Ministry of Education, China), School of Environmental Science and Technology, Dalian University of Technology, Dalian, China. ²College of Environmental Science and Engineering, Dalian Maritime University, Dalian, China. ³Department of Chemistry, Zhejiang University, Hangzhou, China. ⁴Frontier Science Center for Smart Materials, Dalian University of Technology, Dalian, China.

✉ e-mail: liuyanm@dlut.edu.cn

favorable for enhancing hydrogenation and modulating intermediate adsorption is difficult during catalyst synthesis.

Oxide-derived copper (OD-Cu) is a promising catalyst for electrocatalytic reduction¹⁹. Given the strong electron-withdrawing property of oxygen, residual lattice oxygen serves as a negatively charged center in the Cu lattice, which can limit the flow of free electrons, probably weakening $^*\text{NO}_2$ adsorption. However, previous studies have focused on the crystalline phases and facets of OD-Cu catalysts, overlooking the impact of residual lattice oxygen in eNO₃RR. Moreover, OD-Cu has abundant lattice strains due to the oxygen atoms separating out from Cu oxide²⁰. The lattice strains can modulate the activity and product selectivity of electrocatalysts by breaking the linear scaling relationship²¹. Li et al. observed lattice strains in OD-Cu, but their effect on catalysis was not investigated²². It was found later that lattice tensile strains on Cu could lead to hydrogen evolution²³. However, the role of lattice tensile strain in $^*\text{H}$ supply from water splitting hasn't been reported. Meanwhile, the catalytic mechanism of OD-Cu remains insufficiently understood. For example, in situ generated Cu/Cu₂O interface, pure Cu or Cu₂O phase have been reported as active sites for eNO₃RR^{24–27}. The precise active sites are still under debate.

In this work, oxide-derived copper nanosheet arrays (OD-Cu NSs) with residual lattice oxygen and lattice strains were designed to regulate $^*\text{NO}_2$ adsorption strength and $^*\text{H}$ supply during eNO₃RR. The experimental and density functional theory (DFT) results revealed that

residual lattice oxygen modulated the electronic state of the Cu surface, reducing $^*\text{NO}_2$ adsorption and facilitating its conversion. The lattice tensile strains enhanced $^*\text{H}$ supply from water dissociation. The resulted OD-Cu NSs achieved high Faradaic efficiencies (FEs) of 88.7–99.7% for NH_3 production at neutral solution and 50–1500 $\text{mA}\cdot\text{cm}^{-2}$, surpassing the recently reported catalysts. Its potential application has been proved by the efficient recovery of NH_3 and NH_4Cl from NO_3^- reduction.

Results

Synthesis and characterization of OD-Cu NSs

OD-Cu NSs were synthesized on copper foam via chemical oxidation and electrochemical reduction²⁸ (Fig. 1a). The CuO nanosheets were grown on copper foam by oxidation in sodium hydroxide and ammonium persulfate solution. OD-Cu NSs were obtained by electrochemical reduction of CuO nanosheets, in which the reduction potential was determined from its cyclic voltammogram (Supplementary Fig. 1). As a comparison, copper nanosheet arrays (Cu NSs) were prepared by calcination of CuO nanosheets under H_2 . The calcination temperature was selected based on deep removal of lattice oxygen through H_2 -temperature programmed reduction (H_2 -TPR) test (Supplementary Fig. 2). Scanning electron microscopy (SEM) shows the ultrathin and smooth nanosheet morphology of OD-Cu NSs (Fig. 1b and Supplementary Fig. 3). However, the nanosheet surfaces of Cu NSs are rough due to the migration and agglomeration of surface atoms

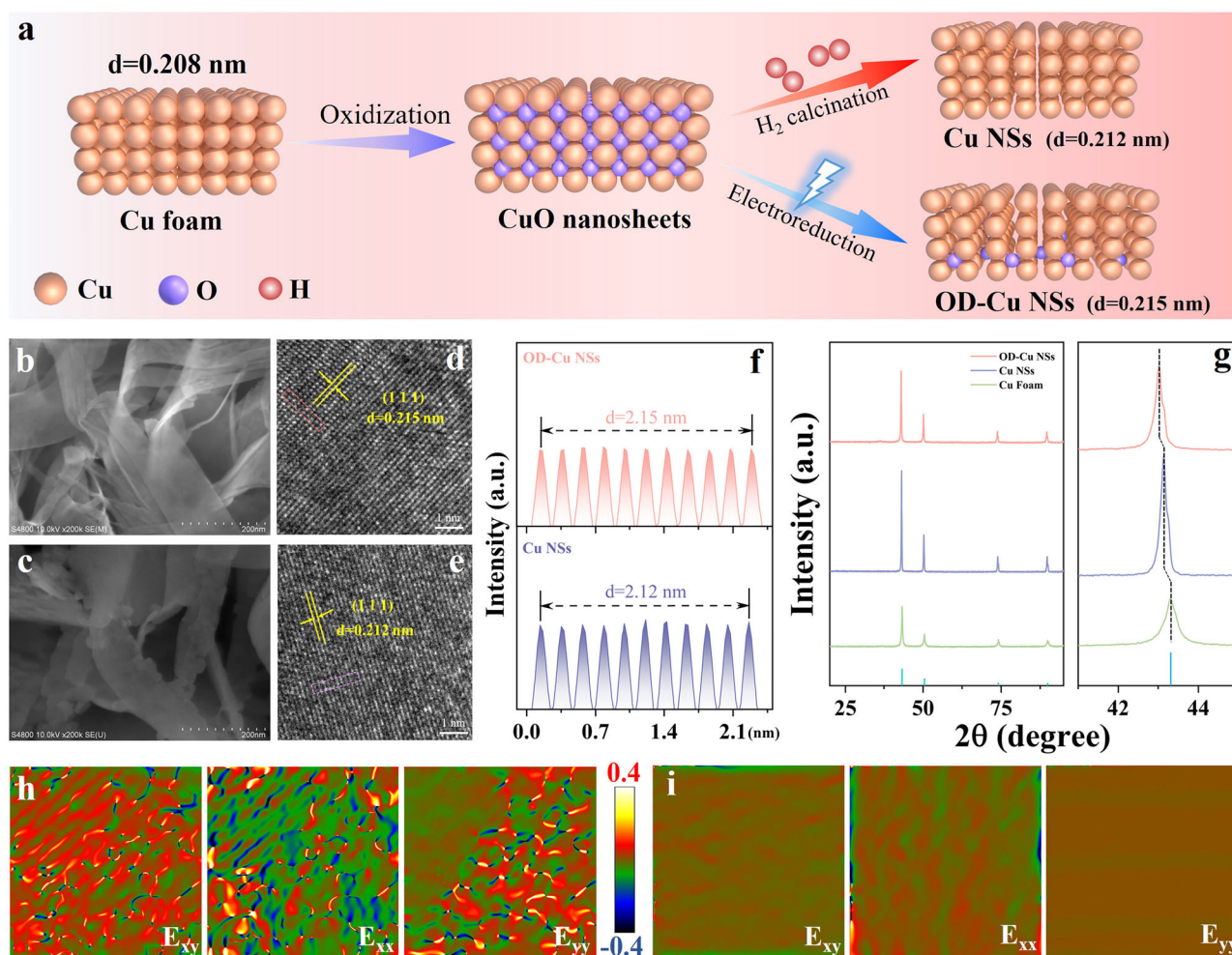


Fig. 1 | Synthetic scheme and morphological characterization. **a** Schematic illustration of Cu NSs and OD-Cu NSs synthesis. **b–e** SEM and HRTEM images of OD-Cu NSs (**b, d**) and Cu NSs (**c, e**), respectively. **f** Lattice spacings of Cu NSs and

OD-Cu NSs. **g** XRD patterns. **h, i** The strain field maps of OD-Cu NSs (**h**) and Cu NSs (**i**) at E_{xy} , E_{xx} , and E_{yy} based on HRTEM images. Source data for Fig. 1 are provided as a Source Data file.

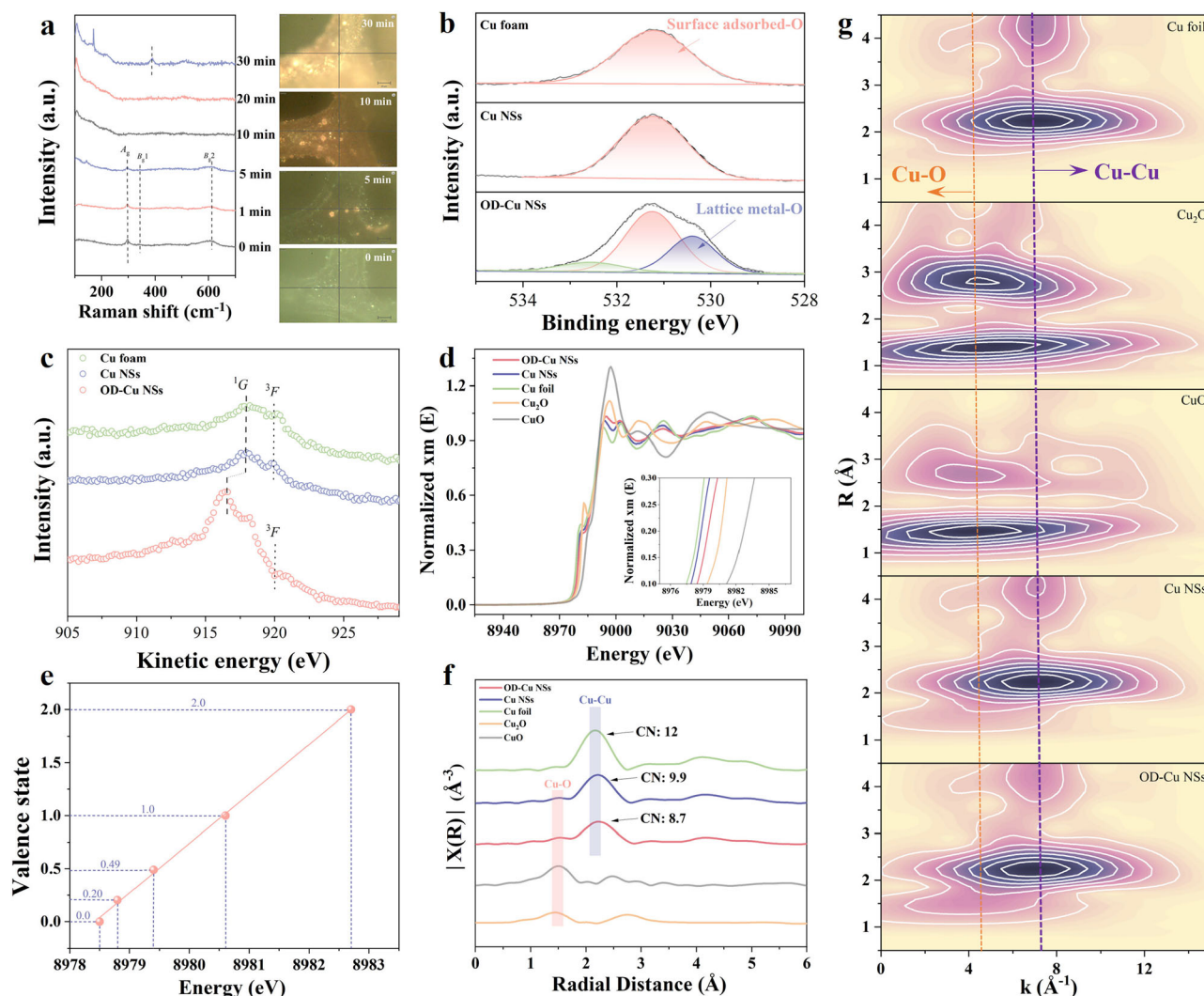


Fig. 2 | Structural characterization. **a** The operando Raman spectra (left panel) and time-resolved light microscopy images (right panel) of OD-Cu NSs surface at -0.87 V. **b** O 1s XPS spectra and **(c)**, Cu $L_{3}M_{45}M_{45}$ Auger spectra of Cu foam, Cu NSs, and OD-Cu NSs. **d** The Cu K-edge XANES spectra. **e** the fitted valence states. **f** the

corresponding k_3 -weighted FT-EXAFS spectra and **(g)**, Morlet WT of the k_3 -weighted EXAFS data for Cu foil, Cu₂O, CuO, Cu NSs, and OD-Cu NSs. Source data for Fig. 2 are provided as a Source Data file.

during thermal reduction²⁹ (Fig. 1c and S3). High-resolution transmission electron microscopy (HRTEM) reveals both OD-Cu NSs and Cu NSs exhibit face-centered cubic (fcc) structures (Fig. 1d and e). Notably, the lattice spacing of the Cu (111) plane is 0.215 nm for OD-Cu NSs (Fig. 1f), which is larger than those of conventional Cu (0.208 nm) and Cu NSs (0.212 nm). The X-ray diffraction (XRD) patterns show the diffraction peaks of Cu NSs and OD-Cu NSs shift to lower angles in comparison to Cu foam (Fig. 1g), reflecting lattice tensile strains in Cu NSs and OD-Cu NSs as determined by the Bragg equation. The OD-Cu NSs have a lower diffraction angle than Cu NSs, which reveals the stronger tensile strains in OD-Cu NSs. The tensile strain value was calculated by the variation of crystal plane spacing. Compared to Cu foam, Cu NSs and OD-Cu NSs have tensile strains of 1.9% and 3.4%, respectively.

The spatial distribution of tensile strains in the catalysts was analyzed by geometric phase analysis. OD-Cu NSs exhibit substantial lattice strains across shear strain (E_{xy}), in-plane strain (E_{xx}), and out-of-plane strain (E_{yy}). Their strain intensities are significantly higher than those in Cu NSs (Fig. 1h and i). This is consistent with the results of XRD and HRTEM. The tensile strains of Cu NSs may originate from the new bond formation, bond breaking, or bond elongation/deflection during the formation of nanosheets³⁰. The more pronounced lattice strains in

OD-Cu NSs are likely due to the escape of oxygen atoms that bound to tetrahedral interstitial sites, leading to further lattice expansion.

Time-resolved operando Raman spectroscopy was used to monitor the oxidation state of the catalyst surface during electro-reduction in the catalyst preparation process (Fig. 2a and Supplementary Fig. 4). The color of OD-Cu NSs surface gradually changes from its initial turquoise (CuO) to bright yellow (Cu) after reduction at -0.87 V (vs RHE) in Na₂SO₄ electrolyte. The Raman spectra at 0 min clearly show three peaks at 297, 343, and 614 cm⁻¹, corresponding to the A_g, B_g1, and B_g2 modes of CuO³¹. As the reduction proceeds, the intensities of CuO peaks gradually decrease until the CuO phase completely disappears at 10 min. Notably, a new band at around 390 cm⁻¹ is observed as the reduction continues, which corresponds to a multi-phonon process of lattice oxygen in Cu. It indicates the presence of residual lattice oxygen and the possible formation of a new Cu suboxide phase³². Moreover, the O 1s XPS spectra (Fig. 2b) show that only surface-adsorbed oxygen is present in Cu foam and Cu NSs, whereas OD-Cu NSs exhibit a lattice metal-oxygen bond around 530.6 eV, confirming the presence of lattice oxygen in OD-Cu NSs³³. Its lattice oxygen content is estimated to be 10.08 at%. The valence state of Cu can be determined from the positions of ¹G and ³F peaks in the Cu Auger spectrum ($L_{3}M_{45}M_{45}$ transition). The ¹G peaks for Cu²⁺, Cu⁺, and

Cu⁰ are usually located at 917.1, 915.8, and 918.0 eV, respectively. In addition, the ³F peak is prominent in the spectrum for Cu⁰ but not in the spectra for Cu₂O and CuO³⁴. As shown in Fig. 2c, the ¹G peaks for Cu foam and Cu NSs are located at 918.0 eV with a distinct ³F peak, consistent with the characteristics of Cu⁰. Notably, the ¹G peak for OD-Cu NSs shifts to approximately 916.5 eV, lower than those of Cu⁰ and Cu²⁺ but close to Cu⁺. Furthermore, the ³F peak related to Cu⁰ still appears in OD-Cu NSs. These results suggest that the valence state of OD-Cu NSs is Cu^{δ+} (0 < δ < 1).

X-ray absorption near-edge structure (XANES) spectroscopy was used to investigate the electronic structure and coordination environment of catalysts. As displayed in Fig. 2d, Cu NSs and Cu foil exhibit insignificant differences in the absorption edge and transition intensity, indicating Cu NSs and Cu have similar coordination environments. However, OD-Cu NSs have higher near-edge absorption energy and lower 1s → 4p transition intensity in comparison to Cu foil and Cu NSs, revealing an abnormal *d-p* hybridization in the Cu atoms of OD-Cu NSs³⁵. It can be attributed to the reduced electron density of 4p orbitals caused by the strong electron-withdrawing property of residual lattice oxygen atoms³⁶. In addition, the near-edge absorption energy of OD-Cu NSs is lower than that of Cu₂O with a fitted valence state of 0.49, suggesting a mixed local environment for its Cu atoms (Fig. 2e). In the k³-weighted Fourier-transformed EXAFS (FT-EXAFS) spectra (Fig. 2f), a distinct Cu-O peak (1.5 Å) appears in OD-Cu NSs, confirming the presence of residual lattice oxygen. The peak intensity of the Cu-Cu bond (2.23 Å)³⁷ in OD-Cu NSs is significantly lower than those of Cu foil and Cu NSs, indicating that the Cu-Cu coordination unsaturation of OD-Cu NSs is increased due to the presence of lattice oxygen atoms. Moreover, the Cu-Cu peaks in OD-Cu NSs and Cu NSs are slightly shifted to a larger radial distance, consistent with the existence of lattice tensile strains²³. The Morlet wavelet transform (WT) plots show that both Cu NSs and OD-Cu NSs exhibit the highest peaks at -7 Å⁻¹ (Fig. 2g), corresponding to the Cu-Cu shell. OD-Cu NSs show a distinct Cu-O shell at -4.5 Å⁻¹, further supporting the presence of residual lattice oxygen in OD-Cu NSs. The EXAFS fitting (Supplementary Fig. 5, 6 and Supplementary Table 1) indicates that the Cu-Cu coordination number (CN) in OD-Cu NSs is 8.7, significantly lower than those in Cu NSs (9.9) and Cu foil (12), which can be explained by that the residual lattice oxygen in OD-Cu NSs reduces the saturation of Cu-Cu coordination. In addition, the average coordination number of Cu-O shell in OD-Cu NSs is 1.0 ± 0.2, revealing the partial saturation of Cu atoms by O atoms in OD-Cu NSs.

The eNO3RR performance of OD-Cu NSs

The eNO3RR performance was evaluated in an H-type cell under ambient conditions. Considering the practical scenarios, a neutral Na₂SO₄ electrolyte was selected. The linear sweep voltammograms (LSV) of OD-Cu NSs (Supplementary Fig. 7) show a distinct current response for 10 mM NO₃⁻ at potential more negative than -0.1 V (vs RHE), indicating its good activity for eNO3RR. NO₃⁻ conversion to NH₃ was further evaluated at -0.3 V to -0.8 V. The NH₃ was quantitatively detected by colorimetric method and validated by ¹H-NMR (Supplementary Fig. 8). Notably, the NH₃ yields of OD-Cu NSs are higher than those of Cu NSs and Cu foam under all the applied potentials (Fig. 3a). At -0.7 V, OD-Cu NSs produce NH₃ at the maximum yield of 0.38 mmol·h⁻¹·cm⁻², which is 1.4 times higher than that of Cu NSs, highlighting the significant role of lattice oxygen and tensile strain in enhancing eNO3RR. The FE_{NH₃} of OD-Cu NSs exhibit a volcano-type trend with the variation of potential (Fig. 3b). At -0.3 V, a high concentration of nitrite is accumulated as *NO₂ can't be efficiently converted, resulting in low FE_{NH₃} (Fig. 3c). As expected, its FE_{NH₃} is significantly increased, and nitrite is rapidly converted at more negative potentials. At -0.6 V, the FE_{NH₃} of OD-Cu NSs is 99.7%, significantly higher than those of Cu NSs (74.2%) and Cu foam (44.2%). The FE of NO₂⁻ is only 1.1% for OD-Cu NSs, much lower than 25.3% for Cu NSs and

28.7% for Cu foam (Fig. 3d and Supplementary Fig. 9). The NO₂⁻ concentration of OD-Cu NSs is also significantly lower than those of Cu NSs and Cu foam (Supplementary Fig. 10). It suggests that OD-Cu NSs can effectively promote nitrite conversion and alleviate *NO₂ poison at the active sites. The generation of byproducts such as NH₂OH, N₂H₄, and NO_x is negligible for eNO3RR on OD-Cu NSs based on the results of online differential electrochemical mass spectrometry (DEMS) and colorimetric methods (Supplementary Fig. 11–14). Considering that OD-Cu NSs and Cu NSs have similar morphology and crystalline structure, the better performance of OD-Cu NSs can be contributed from its residual lattice oxygen and tensile strains, which increase the active sites and result in higher electrochemical active surface area (Supplementary Fig. 15, 16). The FE_{NH₃} of OD-Cu NSs decreases at more negative potentials due to the occurrence of hydrogen evolution. In addition, OD-Cu NSs are also efficient for NH₃ production at lower electrolyte concentrations (0.05–0.1 M) with FE_{NH₃} of 91.2–96.7% (Supplementary Fig. 17). To assess the denitrification performance of OD-Cu NSs, a batch test of NO₃⁻ conversion was conducted at -0.6 V. As shown in Fig. 3e, almost all the nitrogen (10 mM NO₃⁻) is converted to NH₃ after 75 min, and the concentrations of NO₃⁻-N (0.80 ppm) and NO₂⁻-N (4.16 ppm) are well below the World Health Organization's (WHO's) drinking water standards³⁸. The isotope labeling eNO3RR experiment was performed by using K¹⁵NO₃ as a nitrogen source (Fig. 3f). The quantitative results for ¹⁵NH₄⁺ were almost identical to those for ¹⁴NH₄⁺ from ¹⁴NO₃⁻ reduction (Supplementary Fig. 18), which proves that NH₃ is generated from NO₃⁻ reduction instead of other nitrogen sources.

Nitrate concentrations usually vary from ten to more than a hundred millimole per liter in industrial wastewaters^{39,40}. It is crucial for the catalyst to exhibit excellent nitrate-to-ammonia conversion performance across a wide range of NO₃⁻ concentrations. Herein NH₃ synthesis performance of OD-Cu NSs was further explored under 10–140 mM NO₃⁻. The LSV curves show that the current density remarkably increases with the rise of NO₃⁻ concentration (Fig. 3g), indicating the good eNO3RR performance of OD-Cu NSs across a broad range of NO₃⁻ concentrations. Its NH₃ synthesis from 10–140 mM NO₃⁻ was examined at 50–1500 mA·cm⁻², considering that FE_{NH₃} normally declines under high current density⁴¹. As shown in Fig. 3h, OD-Cu NSs maintain high FE_{NH₃} across a wide range of NO₃⁻ concentrations, exceeding 88.7% even at a current density above 1000 mA·cm⁻². Furthermore, both the NH₃ yield and denitrification capability are improved with increasing NO₃⁻ concentration and current density. At 140 mM NO₃⁻ and 1500 mA·cm⁻², the FE_{NH₃} is 88.9% with NH₃ yield of 6.20 mmol·h⁻¹·cm⁻² (105.44 mg·h⁻¹·cm⁻²) and NO₃⁻ removal rate of 91.87 mg·h⁻¹·cm⁻² NO₃⁻-N. Notably, OD-Cu NSs outperform the recently reported electrocatalysts with higher NH₃ yield while keeping an equal or even higher FE_{NH₃} under similar conditions (10–100 mM NO₃⁻, Supplementary Table 2). Meanwhile, OD-Cu NSs keep high FE for NH₃ production during 14 h of NO₃⁻ reduction (10 mM, Fig. 3i and Supplementary Fig. 19), demonstrating the good durability of OD-Cu NSs for NH₃ synthesis. After the stability test, OD-Cu NSs retain the initial nanosheet morphology and lattice strains (Supplementary Fig. 20a, b). Furthermore, XPS and Cu L₃M₄₅M₄₅ Auger spectra prove the well-maintained lattice oxygen and Cu valence state after 14 cycles of eNO3RR, which reveals its good stability (Supplementary Fig. 20c, d). Meanwhile, in situ Raman spectra confirm the well-maintained lattice oxygen for OD-Cu NSs (Supplementary Fig. 21). The OD-Cu NSs are stable for eNO3RR without structure reconstruction.

The catalytic mechanism of OD-Cu NSs

The reduction of NO₃⁻ to NH₃ involves a complex 8 electrons and 9 protons transfer process. For Cu-based catalysts, there are significant challenges in the conversion and hydrogenation of intermediates such as *NO₂, leading to limited eNO3RR performance⁴². To investigate the

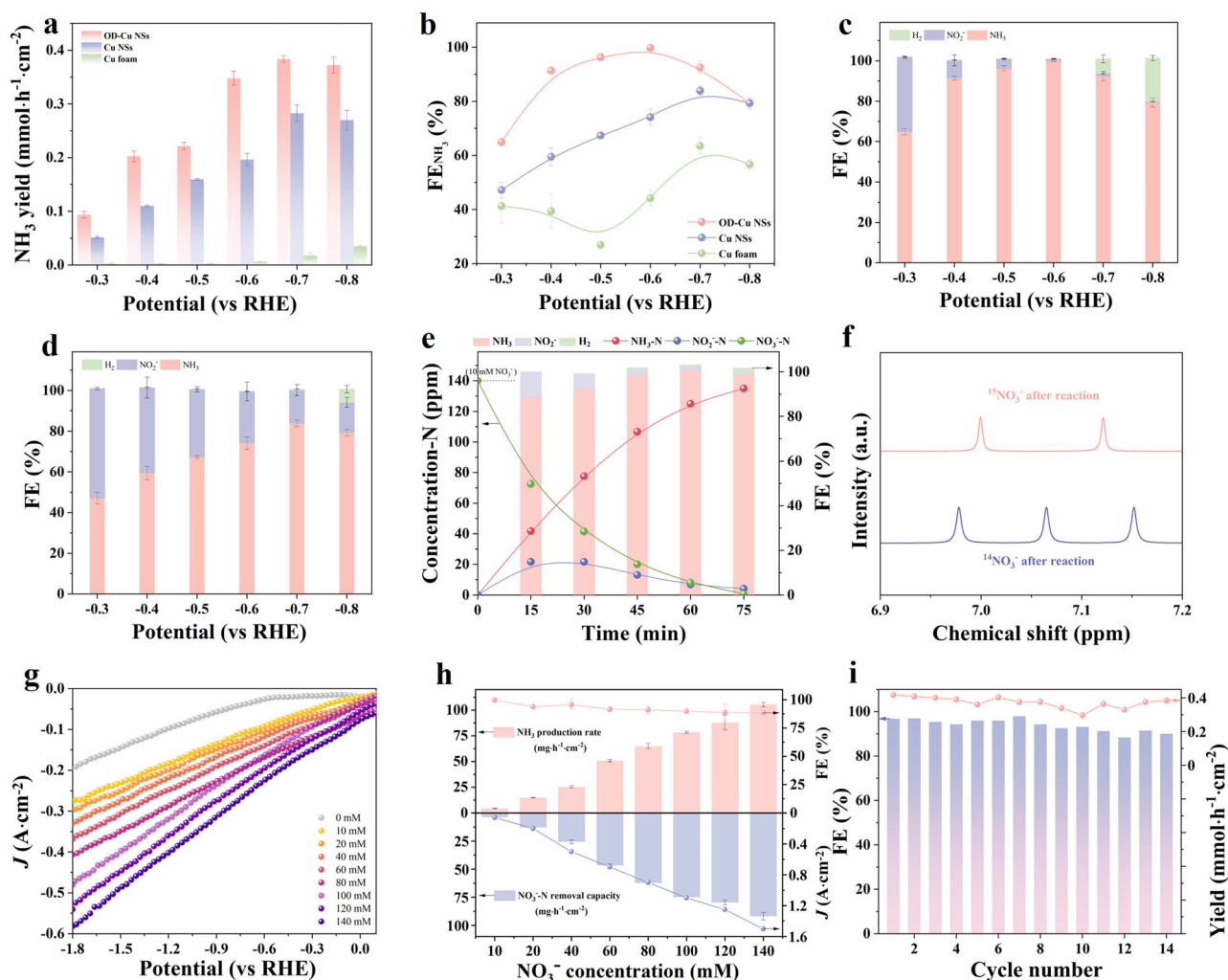


Fig. 3 | Performance for eNO₃RR. a NH_3 yields and **(b)**, corresponding FEs for 10 mM NO_3^- reduction on Cu foam, Cu NSs, and OD-Cu NSs. **(c, d)** The product distribution for OD-Cu NSs **(c)** and Cu NSs **(d)**. **(e)** Time-dependent concentrations of NO_3^- , NO_2^- , and NH_3 during the reduction of 10 mM NO_3^- over OD-Cu NSs. **(f)** ^1H NMR spectra of samples from OD-Cu NSs catalyzed $^{15}\text{NO}_3^-$ or $^{14}\text{NO}_3^-$ reduction. **(g)** LSV

curves and **(h)**, nitrate removal capacities and NH_3 production rates of OD-Cu NSs at 10–140 mM NO_3^- . **(i)** Stability of OD-Cu NSs for 14 successive cycles of 10 mM NO_3^- reduction at -0.6 V (Na_2SO_4 electrolyte). Error bars represent the standard deviation from three independent measurements. All the potentials have not been iR-corrected. Source data for Fig. 3 are provided as a Source Data file.

ability of OD-Cu NSs for the conversion of intermediates, the rate constants for NO_3^- conversion to NO_2^- (k_1 , Supplementary Fig. 22, 23) and NO_2^- conversion to NH_3 (k_2 , Supplementary Fig. 24, 25) were calculated to assess the reaction kinetics⁷. Meanwhile, the onset potentials for NO_3^- and NO_2^- reduction on OD-Cu NSs, Cu NSs, and Cu foam were compared (Supplementary Fig. 26). As can be seen from Fig. 4a, OD-Cu NSs have the highest k_1 and k_2 values among the three catalysts, which proves that OD-Cu NSs can realize rapid $\text{NO}_3^- \rightarrow \text{NO}_2^-$ and $\text{NO}_2^- \rightarrow \text{NH}_3$ conversion. Notably, OD-Cu NSs have the lowest onset potential for NO_2^- reduction, which further demonstrates its excellent NO_2^- conversion performance. This may be attributed to the presence of residual lattice oxygen, which limits free electrons on the Cu surface and facilitates $^*\text{NO}_2$ desorption and conversion (Fig. 4b, right panel). To illustrate the influence of lattice oxygen on $^*\text{NO}_2$ conversion, OD-Cu with lattice oxygen and tensile strain of 1.9% (OD-Cu_{oxide}) was prepared (Supplementary Fig. 27a, b). The OD-Cu_{oxide} has the same tensile strain value as Cu NSs, but it exhibits significantly higher FE_{NH_3} and lower nitrite accumulation than Cu NSs for eNO₃RR under the same conditions (Supplementary Fig. 27c, d), demonstrating the crucial role of lattice oxygen in promoting $^*\text{NO}_2$ conversion and NH_3 production. Although Cu NSs have a lower onset potential for NO_3^- reduction than OD-Cu NSs, its k_1 and k_2 values are lower than those of OD-Cu NSs. This

may be caused by that the metallic property of Cu NSs favors NO_3^- reduction, but the generated NO_2^- poisons the active sites and reduces the reaction rate (Fig. 4b, left panel). For Cu foam, both NO_3^- and NO_2^- reduction require high overpotentials with the lowest k_1 and k_2 values. This is consistent with its worst eNO₃RR performance.

The in situ ATR-FTIR spectroscopy was employed to probe the dynamic evolution of intermediates generated from eNO₃RR on OD-Cu NSs (Supplementary Fig. 28). As shown in Fig. 4c, the characteristic peak at 1650 cm^{-1} corresponds to the bending vibration of $^*\text{H}_2\text{O}$ in the thin electrolyte layer⁴³. Concurrently, the strong absorption peak at 3390 cm^{-1} is attributed to the $^*\text{O-H}$ stretching. It implies that OD-Cu NSs are favorable for the adsorption and decomposition of water to produce $^*\text{H}$. The band at 3250 cm^{-1} can be assigned to $^*\text{NH}_2$ bending⁴⁴. The intermediate at -1430 cm^{-1} is attributed to $^*\text{NH}_2\text{OH}$, a key intermediate for NH_3 formation⁴³. Meanwhile, the downward band at 1240 cm^{-1} belongs to $^*\text{NO}_2$. As the potential is shifted from -0.3 V to -0.7 V, the peak intensity of $^*\text{NO}_2$ increases gradually and suddenly flattens out at -0.7 V, indicating that $^*\text{NO}_2$ undergoes a rapid conversion. It is noteworthy that the ratio of $^*\text{NO}_2$ peak area to the total area of $^*\text{NO}_2$ and $^*\text{NH}_2\text{OH}$ decreases sharply with the potential negatively shifted (Fig. 4d). Meanwhile, the peak intensity of $^*\text{NH}_3$ (1100 cm^{-1}) exhibits a progressive enhancement at more negative potentials.

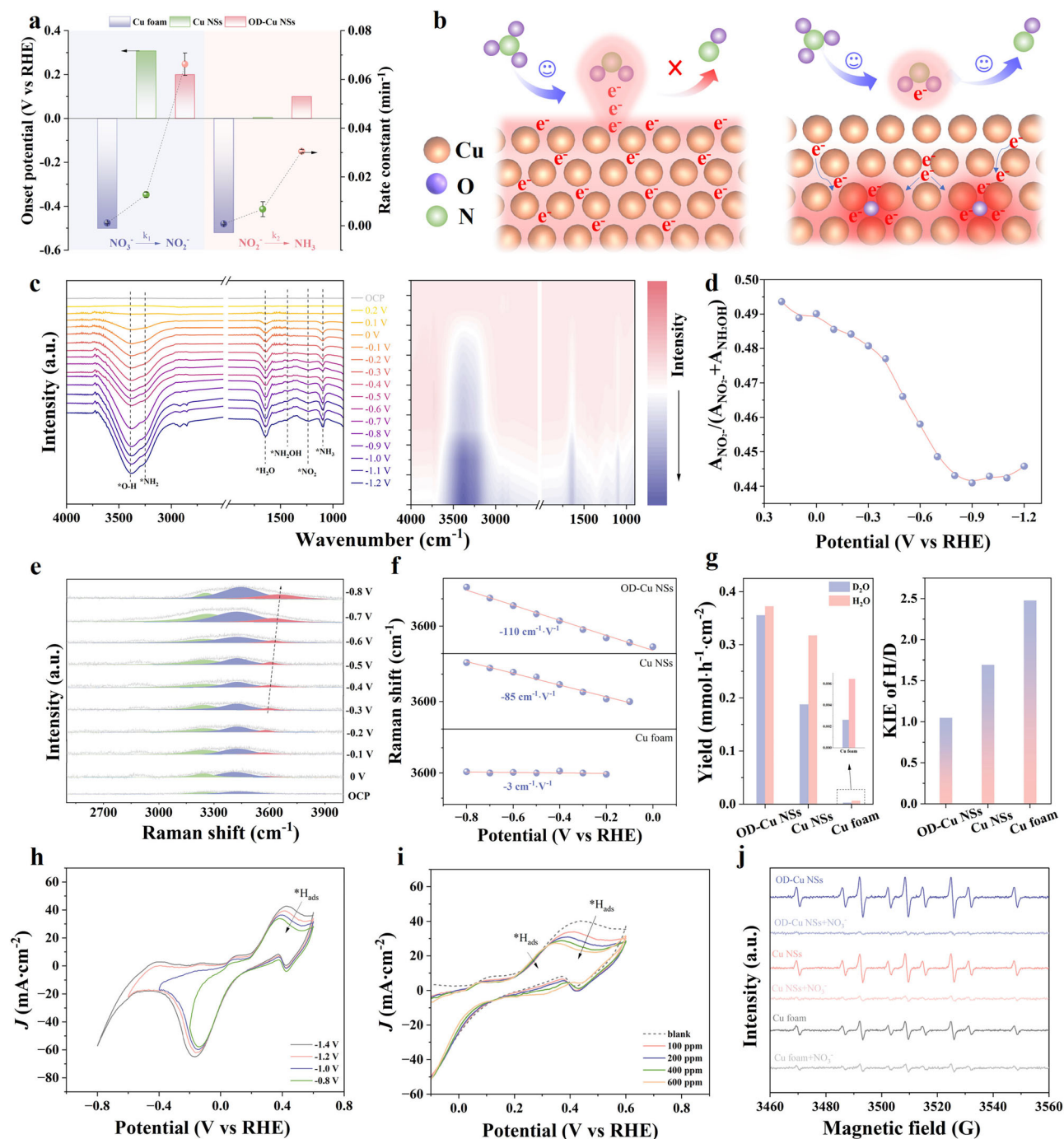


Fig. 4 | Mechanism analysis for $^*\text{NO}_2$ conversion and $^*\text{H}$ generation. **a** The onset potentials and reaction constants for NO_3^- conversion to NO_2^- (k_1) and NO_2^- conversion to NH_3 (k_2) on OD-Cu NSs, Cu NSs, and Cu foam in 0.5 M Na_2SO_4 + 10 mM $\text{NO}_3^-/\text{NO}_2^-$ (Error bars represent standard deviation from three independent measurements). **b** Schematic diagram of lattice oxygen-mediated intermediate adsorption on Cu surface. **c** The operando ATR-FTIR spectra and 2D FTIR contour map. **d** the $\text{ANO}_2/(\text{ANO}_2 + \text{ANH}_2\text{OH})$ and **(e)**, in situ Raman spectra of different interfacial water during eNO₃RR on OD-Cu NSs at different potentials.

f Wavenumber shift of dangling O-H with potential changes. **g** NH_3 yields and KIE values for eNO₃RR at -0.6 V using H_2O and D_2O as solvents. Cyclic voltammograms of OD-Cu NSs in **(h)**, Ar-saturated 0.5 M Na_2SO_4 under different starting potentials and **(i)**, different NO_3^- concentrations. **j** EPR spectra of $^*\text{H}$ signal for OD-Cu NSs, Cu NSs, and Cu foam with and without the presence of nitrate (-0.6 V). All the potentials have not been iR-corrected. Source data for Fig. 4 are provided as a Source Data file.

However, both Cu NSs and Cu foam exhibit distinct $^*\text{NO}_2$ signals, and the peak intensity of $^*\text{NO}_2$ almost keeps unchanged with the negative shift of potential (Supplementary Fig. 29). These results indicate that OD-Cu NSs are more efficient for converting $^*\text{NO}_2$ to NH_3 .

The $^*\text{H}$ supply from water dissociation is a key step for NH_3 production in neutral solution⁴⁵. In situ Raman spectroscopy was used to analyze the water peak at 2800–4000 cm^{-1} . By Gaussian fitting of the

interfacial water peak, tetrahedrally coordinated H_2O (tetra- H_2O , 3230 cm^{-1}), trihedrally coordinated H_2O (tri- H_2O , 3425 cm^{-1}) and dangling O-H bond (3600 cm^{-1}) of H_2O ⁴⁶ can be found. The dangling O-H is a weak hydrogen bond configuration, which tends to adsorb on the catalyst surface and dissociate to generate $^*\text{H}$. Its position is red-shifted as the potential decreases (Fig. 4e), indicating preferential dissociation of dangling O-H on OD-Cu NSs⁴⁷. A weaker shift of the dangling O-H

peak under more negative potential is observed on Cu NSs, and a negligible shift is observed on Cu foam compared to OD-Cu NSs (Supplementary Fig. 30, 31). It is noteworthy that the slopes of dangling O-H peak displacement show a trend of OD-Cu NSs ($-110 \text{ cm}^{-1} \cdot \text{V}^{-1}$) > Cu NSs ($-85 \text{ cm}^{-1} \cdot \text{V}^{-1}$) > Cu foam ($-3 \text{ cm}^{-1} \cdot \text{V}^{-1}$) (Fig. 4f), suggesting that OD-Cu NSs are more conducive to $^*\text{H}$ generation from water dissociation. OD-Cu NSs and Cu NSs display significantly enhanced ability for water dissociation to $^*\text{H}$ relative to Cu foam. Both Cu NSs and Cu foam don't contain lattice oxygen, but Cu NSs have tensile strains compared to Cu foam. It is reasonable to speculate that tensile strains play a key role in enhancing $^*\text{H}$ supply from water dissociation.

The kinetic isotope effect (KIE) of H/D ($\text{H}_2\text{O}/\text{D}_2\text{O}$) for eNO3RR was further examined to validate the role of lattice tensile strains in accelerating H_2O dissociation. The KIE value is a good indicator of proton transfer kinetics, providing insights into the rate-determining step (RDS). KIE > 1 indicates that proton transfer is involved in the RDS, while KIE ≈ 1 suggests proton transfer is not a limiting factor⁴⁸. As shown in Fig. 4g, the NH_3 yield of Cu foam is significantly decreased after the replacement of H_2O by D_2O and its KIE value is 2.47, indicating the limited proton supply for eNO3RR. Cu NSs show a smaller change in NH_3 yield and current density after the replacement of H_2O by D_2O (Supplementary Fig. 32) and a KIE value of 1.69, suggesting that the proton supply capacity of Cu NSs is enhanced by the introduction of tensile strains. Interestingly, the NH_3 yield and current density (Supplementary Fig. 33) of OD-Cu NSs almost keep unchanged after the replacement of H_2O by D_2O , and its KIE value is only 1.05. This phenomenon may be due to the fact that OD-Cu NSs have stronger tensile strains, which promotes water dissociation and provide sufficient $^*\text{H}$ for hydrogenation. Moreover, the linear relationship between tensile strain and KIE value further confirms that tensile strain accelerates $^*\text{H}$ generation (Supplementary Fig. 34). The $^*\text{H}$ generation ability of catalysts was investigated by measuring $^*\text{H}_{\text{ads}}$ peak intensity via cyclic voltammogram at different initial potentials⁴⁹. OD-Cu NSs exhibit stronger $^*\text{H}_{\text{ads}}$ peak intensity and larger intensity enhancement than Cu NSs as the applied potential decreases, whereas negligible $^*\text{H}_{\text{ads}}$ peak appears for Cu foam (Fig. 4h and Supplementary Fig. 35, 36). It further confirms the vital role of tensile strain in promoting $^*\text{H}$ generation. By increasing the NO_3^- concentration for cyclic voltammogram test, the $^*\text{H}_{\text{ads}}$ intensity on OD-Cu NSs is reduced obviously (Fig. 4i), indicating that $^*\text{H}$ plays a crucial role in promoting NO_3^- reduction. Its good $^*\text{H}$ generation and utilization ability is also proved by EPR spectra (Fig. 4j). OD-Cu NSs exhibit stronger $^*\text{H}$ signal intensity than Cu NSs and Cu foam (-0.6 V). Its $^*\text{H}$ signal almost disappears after the addition of nitrate. In contrast, the $^*\text{H}$ consumption is slower for Cu NSs and Cu foam. It confirms the accelerated $^*\text{H}$ supply and utilization of OD-Cu NSs for nitrate reduction.

Density functional theory (DFT) calculation was employed to further elucidate the mechanism of residual lattice oxygen and lattice strain for regulating the eNO3RR activity of OD-Cu NSs. Based on the good matching between FT-EXAFS data of OD-Cu NSs and the simulated EXAFS result of atypical suboxide copper in previous works⁵⁰, we constructed the OD-Cu model (Cu_4O) (Supplementary data 1). To investigate the impact of residual lattice oxygen on eNO3RR, the tensile strain was not introduced into the computational model. The impact of residual lattice oxygen on the electronic state of the Cu surface was investigated (Supplementary Fig. 37). As shown in the electron localization function (ELF) map (Fig. 5a), the surface electrons on OD-Cu that contain residual lattice oxygen are more localized compared to those on Cu surface⁵¹. It implies that the valence electrons in OD-Cu are less free to move across the surface, thereby weakening the electronic coupling between the catalyst surface and $^*\text{NO}_2$. This is conducive to reduce adsorption strength of $^*\text{NO}_2$ intermediate. The applied potential has insignificant influence on the electronic structures of OD-Cu and Cu under the investigated conditions

(Supplementary Fig. 38). The adsorption energy of $^*\text{NO}_2$ on OD-Cu and Cu surface were further calculated (Supplementary Fig. 39). As depicted in Fig. 5b, the adsorption of $^*\text{NO}_2$ on OD-Cu surface (-1.28 eV) is weaker than that on Cu surface (-1.62 eV), which is attributed to the strong electron-withdrawing effect of subsurface lattice oxygen on OD-Cu. It diminishes the electron transfer between its surface and the $^*\text{NO}_2$ (Fig. 5c), thus alleviating the poison of active sites.

To explore the influence of tensile strain on $^*\text{H}$ generation from water dissociation, DFT calculation was conducted on the models of Cu (111) with 0%, 1.9%, and 3.4% lattice tensile strains (denoted as Cu-0%, Cu-1.9%, and Cu-3.4%) based on the tensile strains observed in OD-Cu NSs and Cu NSs (Supplementary Fig. 40–43 and Supplementary data 1). The water adsorption energy is -0.37 eV for Cu-0%, which decreases to -0.48 eV for Cu-1.9% and -0.82 eV for Cu-3.4%. Water adsorption is facilitated on the Cu surface with the rise of tensile strains. It may be due to the altered electronic structure by the increased tensile strains, leading to an upward shift of its d -band center (Supplementary Fig. 44). The upshifted d -band center strengthens the interaction between the catalyst surface and water, improving the adsorption of water molecules. The facilitated water adsorption favors subsequent water dissociation to produce $^*\text{H}$. As shown in Fig. 5d, Cu-3.4% exhibits a low energy barrier ($\Delta G^*\text{H}_2\text{O} = 0.11 \text{ eV}$) for H_2O dissociation to $^*\text{H}$, while $\Delta G^*\text{H}_2\text{O}$ increases to 0.22 eV for Cu-1.9% and 0.32 eV for Cu-0%, indicating that larger tensile strains are more favorable for $^*\text{H}$ generation. In addition, the protonation of the surface oxygen atoms of OD-Cu is thermodynamically unfavorable in comparison with eNO3RR (Supplementary Fig. 45), which is unlikely to influence $^*\text{NO}_2$ conversion and water decomposition. Both theoretical and experimental results confirm that the electronic modulation mediated by residual lattice oxygen effectively promotes $^*\text{NO}_2$ conversion and mitigates active site poison. Concurrently, tensile strains improve the water dissociation capability of Cu, providing sufficient $^*\text{H}$ for hydrogenation. The synergistic effects of residual lattice oxygen and tensile strains enhance NH_3 synthesis on OD-Cu NSs (Fig. 5e).

To explore the reaction pathway for eNO3RR, the reaction intermediates were identified by in situ Raman and DEMS. In the Raman spectra (Supplementary Fig. 46), $^*\text{NO}_3$ stretching peak is observed at 1050 cm^{-1} under open circuit potential (OCP). When negative potential is applied, $^*\text{NO}_3$ peak gradually disappears, while two new Raman bands appear at 1326 cm^{-1} and 1591 cm^{-1} , corresponding to the anti-symmetric stretching of $^*\text{NO}_2$ and $^*\text{NH}_3$, respectively. The signal intensity of $^*\text{NO}_2$ first increases and then disappears with the negative shift of potential. It reveals the generation of $^*\text{NO}_2$ and its transformation to ammonia during eNO3RR. The online DEMS shows a strong signal at $m/z = 17$, which is attributed to NH_3 (Supplementary Fig. 11). The other signals at $m/z = 16, 33, 44, 15$, and 30 can be assigned to NH_2 , NH_2OH , N_2O , NH and NO , respectively. The signal intensities of these intermediates are 1–4 orders of magnitude lower than that of NH_3 , which may be related to the rapid conversion of these intermediates. These results are consistent with in situ ATR-FTIR data in Fig. 4c. Based on the intermediates detected, the eNO3RR pathway and the reaction-free energies on OD-Cu and Cu surfaces were explored by DFT calculation. As shown in Fig. 5f, the reaction begins with the adsorption of NO_3^- onto the catalyst surface, and the formed $^*\text{NO}_3$ is spontaneously converted to $^*\text{NO}_2$ via N-O bond breaking. The $^*\text{NO}_2$ hydrogenation to $^*\text{NO}_2\text{H}$ is an uphill process with the free energy of 0.11 eV on the OD-Cu surface, significantly lower than that on the Cu surface (0.60 eV), highlighting the role of residual lattice oxygen in promoting $^*\text{NO}_2$ conversion and suppressing nitrite accumulation. Subsequently, the $^*\text{NO}_2\text{H}$ is converted to $^*\text{NO}$, followed by $^*\text{NO}$ reduction to $^*\text{NOH}$. The formed $^*\text{NOH}$ is further reduced to $^*\text{NH}_3$ via the pathway of $^*\text{NOH} \rightarrow ^*\text{NHOH} \rightarrow ^*\text{NH}_2\text{OH} \rightarrow ^*\text{NH}_2 \rightarrow ^*\text{NH}_3$ or $^*\text{NOH} \rightarrow ^*\text{N} \rightarrow ^*\text{NH} \rightarrow ^*\text{NH}_2$ (downhill process). NH_3 is generated after $^*\text{NH}_3$ desorption from the catalyst surface. Notably, the rate-determining step (RDS) on OD-Cu is $^*\text{NO} \rightarrow ^*\text{NOH}$. Its energy barrier is 0.37 eV , which is considerably lower than

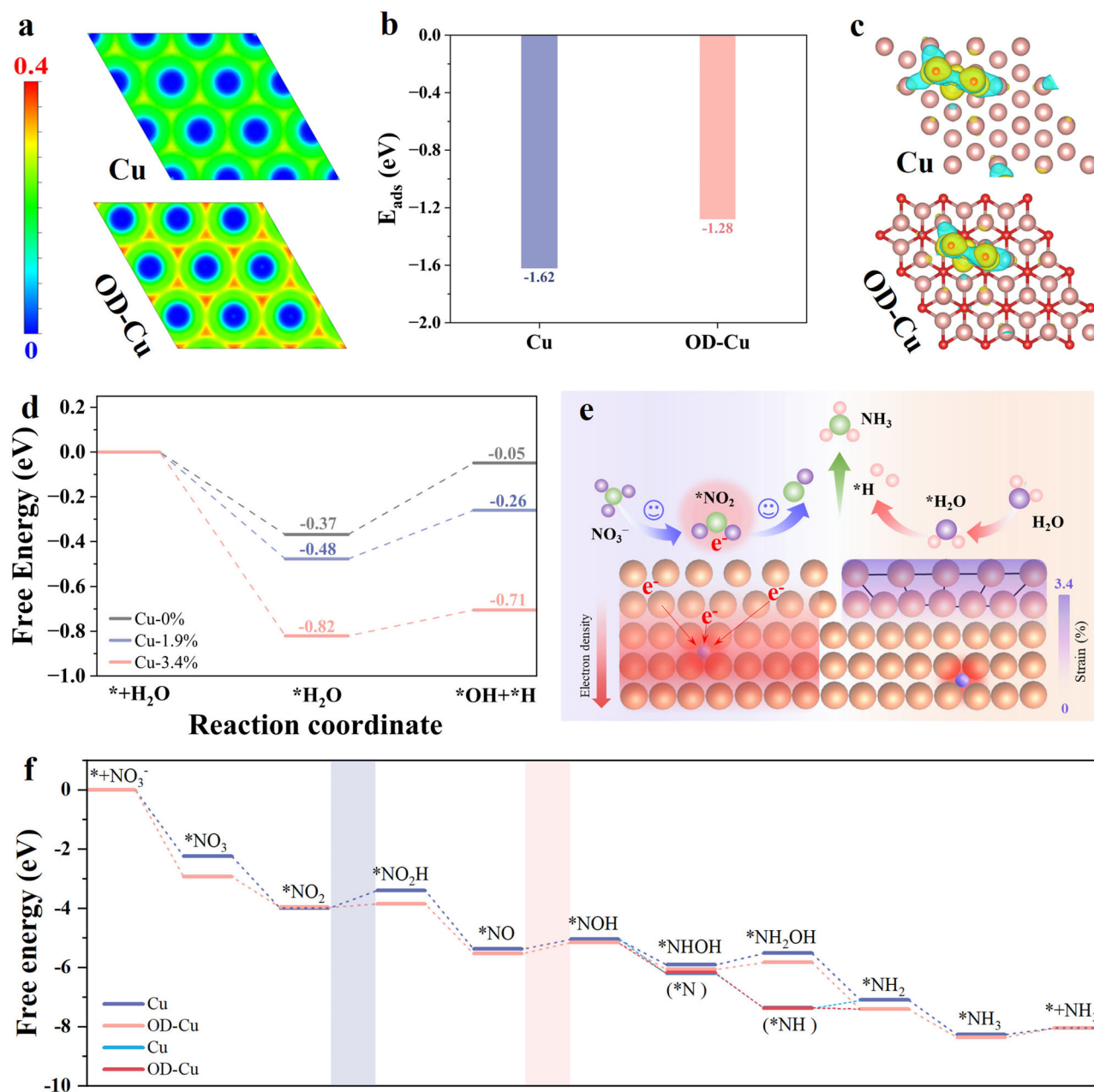


Fig. 5 | Reaction mechanism from DFT calculation. **a** ELF maps and **(b)** adsorption energies of NO_2^- on Cu and OD-Cu surfaces. **c** The adsorption model and charge density difference of Cu and OD-Cu (accumulation and deletion of electrons are shown in blue and yellow). **d** Gibbs free energy for H_2O dissociation to $^*\text{H}$ on Cu-

0%, Cu-1.9% and Cu-3.4% surfaces. **e** Schematic diagram of eNO₃RR promoted by lattice oxygen-mediated electron regulation and lattice strain-mediated water dissociation. **f** Gibbs free energy diagrams for eNO₃RR on the surfaces of Cu and OD-Cu. Source data for Fig. 5 are provided as a Source Data file.

0.60 eV for the RDS of Cu ($^*\text{NO}_2 \rightarrow ^*\text{NO}_2\text{H}$). Meanwhile, the effect of tensile strains on reducing the energy barrier of RDS is insignificant for OD-Cu (Supplementary Fig. 47). These results demonstrate that the lattice oxygen of OD-Cu significantly reduces the energy barrier for eNO₃RR and promotes NH_3 production.

Application for ammonia recovery

Given the excellent eNO₃RR performance of OD-Cu NSs, the conversion of NO_3^- into high-purity, ammonia-based chemicals was explored to assess its potential for practical application. NH_3 in the electrolyte after eNO₃RR (100 mM NO_3^- , -1.1 A cm^{-2}) was extracted via argon stripping at 50 °C (Fig. 6a). Approximately 95.0% of NH_3 vapor is successfully removed from the electrolyte (Fig. 6b), indicating the system is effective for NO_3^- removal and NH_3 recovery. 92.2% of the stripped

NH_3 vapor is captured through an acidic solution (HCl), and 82.9% of high-purity NH_4Cl powder is collected after solvent evaporation (Fig. 6c and Supplementary Fig. 48). This demonstrates the feasibility of OD-Cu NSs-based eNO₃RR system for NH_3 recovery. For eNO₃RR under industrial-scale current density, slow mass transfer and incongruous NH_3 production in static H-cell hinder its large-scale application. Flow cells can enhance mass transfer and provide a stable reaction microenvironment (e.g., local concentration and pH) for continuous NH_3 production compared to H-cell. Therefore, we assembled the OD-Cu NSs catalyst into a membrane electrode assembly (MEA) to investigate its performance and long-term stability for NO_3^- reduction to NH_3 under industrial-scale current. The setup of MEA is illustrated in Supplementary Fig. 49, 50. The total current for long-term operation was set at 1 A. As shown in Fig. 6d, OD-Cu NSs still

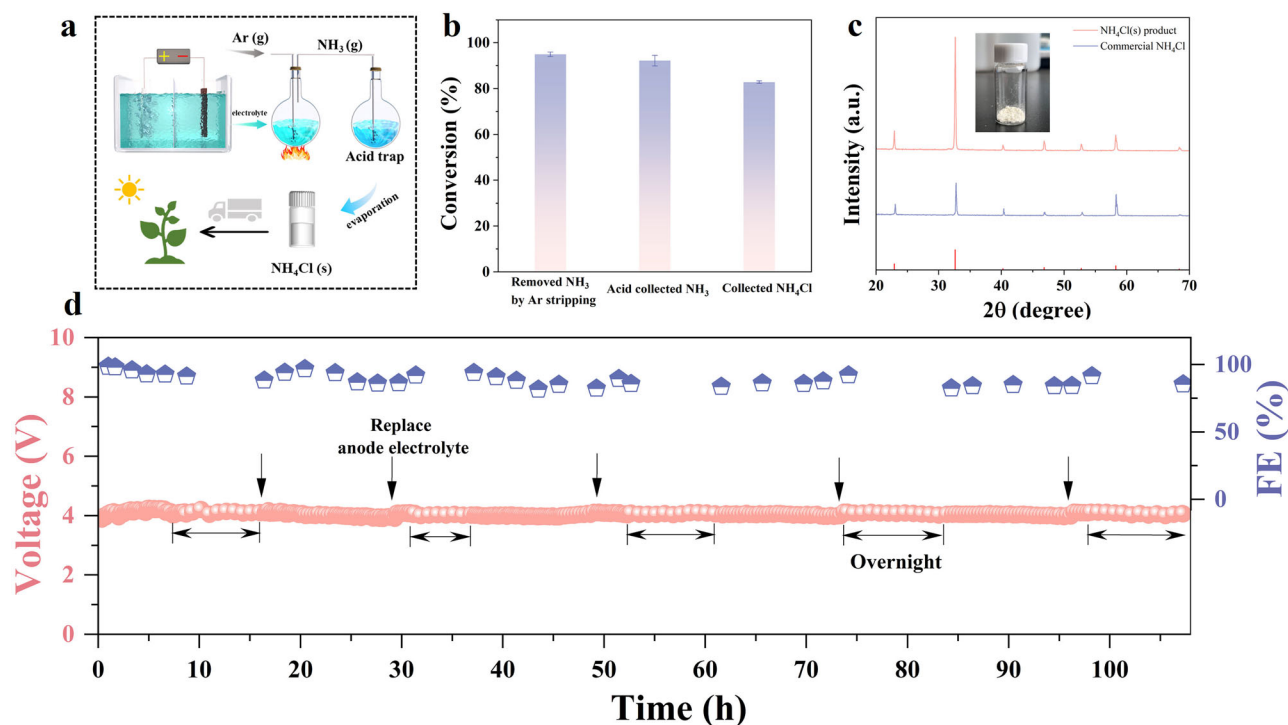


Fig. 6 | Ammonia recovery and stability. **a** Schematic illustration of the process for converting nitrate to high-purity NH₄Cl. **b** The conversion efficiency for NH₃ synthesis from the reduction of 100 mM NO₃[−] at −1.1 A cm^{−2} (Error bars represent standard deviation from three independent measurements). **c** XRD pattern of the

synthesized NH₄Cl product. **d** Long-term stability for eNO₃RR over OD-Cu NSs using a MEA system (30 mM NO₃[−], 1.0 A, 4.0 cm², Na₂SO₄ electrolyte). Source data for Fig. 6 are provided as a Source Data file.

achieve a FE_{NH₃} of 98.6% and NH₃ yield of 1.15 mmol·h^{−1}·cm^{−2} in the MEA system (30 mM NO₃[−]). The FE_{NH₃} and NH₃ yield remain ~90% of initial values with negligible potential decay after 100 h of operation, demonstrating the good stability of OD-Cu NSs for NH₃ synthesis. Techno-economic analysis shows that NH₃ electrosynthesis from nitrate wastewater is economically and technically feasible on OD-Cu NSs-based MEA system (Supplementary Fig. 51 and Supplementary Note 1). The effluent from the MEA was subjected to NH₃ separation and conversion. The mass flow and product distribution of eNO₃RR are shown in Supplementary Fig. 52. After eNO₃RR, the nitrate removal rate reaches 98%, and 84% of nitrate is converted to NH₄Cl, illustrating its applicability for scaled applications in nitrate wastewater treatment and resource utilization.

Discussion

OD-Cu NSs with residual lattice oxygen and lattice tensile strains were prepared by a simple method. The OD-Cu NSs demonstrated remarkable eNO₃RR activity and stability with nearly 100% FE_{NH₃} at 10 mM NO₃[−] and neutral solution. It was also efficient for NH₃ electrosynthesis with FE_{NH₃} of 88.7–99.7% and maximum NH₃ yield of 6.20 mmol·h^{−1}·cm^{−2} across a wide range of NO₃[−] concentrations (10–140 mM) at 50–1500 mA·cm^{−2}. It converted over 80% of 100 mM NO₃[−] into high-purity NH₄Cl. The superior performance of OD-Cu NSs was attributed to electron regulation mediated by residual lattice oxygen and water dissociation mediated by lattice strains, which accelerated *NO₂ conversion and *H supply for NH₃ synthesis from eNO₃RR. This work broadens the mechanistic understanding and will open up new possibilities for enhancing electrocatalytic performance in other fields.

Methods

Chemicals

Cu foam (thickness: 2.0 mm) was purchased from Suzhou Keshenghe Metal Material Co., Ltd. Ammonium persulphate ((NH₄)₂S₂O₈, AR 98%)

and Sodium hydroxide (NaOH, AR 99.9%) were obtained from Aladdin. All the chemicals were received and used without further purification. Deionized water (18.25 mΩ·cm^{−1}) was used in all experiments.

Synthesis of OD-Cu NSs, Cu NSs and OD-Cu_{oxide}

In a typical procedure, Cu foam was ultrasonically treated with 1 M hydrochloric acid and anhydrous ethanol for 15 min each to remove surface impurities. The Cu foam was then rinsed thoroughly with ultrapure water, dried under vacuum, and stored for later use. To prepare the oxidation solution, 16 g of sodium hydroxide was dissolved in ultrapure water (70 mL). Subsequently, 3.2 g of ammonium persulfate was added to the sodium hydroxide solution and dissolved using ultrasound treatment. The Cu foam was immersed in the prepared solution and oxidized at 60 °C for 20 min. After oxidation, the Cu foam was rinsed with ultrapure water, and CuO nanosheets were obtained. The OD-Cu NSs were prepared by electrochemical reduction of CuO nanosheets for 30 min in 0.5 M Na₂SO₄ electrolyte at −0.87 V vs RHE (All the potentials have not been iR-corrected in this work). As comparison, Cu NSs were prepared by annealing CuO nanosheets at 350 °C for 2 h under 10% H₂/Ar atmosphere. OD-Cu_{oxide} was prepared through direct pyrolysis of copper foam (450 °C for 2 h under Ar), followed by electrochemical reduction under the same conditions as OD-Cu NSs preparation.

Characterization

The morphology and structure of catalysts were examined using a scanning electron microscope (Hitachi S4800) and a transmission electron microscope (FEI Talos F200S). X-ray photoelectron spectroscopy (XPS) data were acquired with an ESCALAB 250Xi spectrometer. All spectra were calibrated by setting the C 1s peak to 284.8 eV. Raman spectra were recorded on a Renishaw inVia Qontor confocal Raman spectrometer using a 633 nm laser. X-ray diffraction (XRD) patterns were collected on a Rigaku Ultima IV diffractometer. ¹H NMR spectra

were obtained using a BRUKER AVANCE NEO 600 M spectrometer. Ultraviolet-visible (UV-Vis) absorbance spectra were measured with a SP-756P spectrophotometer. The TPR-H₂ experiment was carried out on an Autochem II 2920-MKS CirrusTM 3.

In situ, Raman measurements were performed using a customized Raman reaction cell and a CHI 760E electrochemical workstation. The conditions for the Raman test were the same as those of electrochemical tests, except that the electrolytes (50 mL) for the cathode and anode chambers were circulated outside the cell using a peristaltic pump.

In situ attenuated total reflection Fourier-transform infrared (ATR-FTIR) spectroscopy was conducted using a Thermo Scientific iS50 FT-IR instrument equipped with a mercury cadmium telluride (MCT) detector. The experiments employed a custom-made infrared cell connected to a CHI 760E electrochemical workstation. The electrolyte solution consisted of 0.5 M Na₂SO₄ and 0.1 M KNO₃. After subtracting the infrared background, spectra were recorded under applied potentials with Ag/AgCl as the reference electrode and platinum (Pt) as the counter electrode. The applied potential was from 0.2 V to −1.2 V.

The H₂-TPR experiment was conducted on an Autochem II instrument. OD-Cu NSs were loaded into a quartz tube and pretreated by sweeping with Ar at 120 °C for 30 min to remove any adsorbed species. After cooling to 25 °C, the temperature was increased to 600 °C at a rate of 10 °C min^{−1} under a gas mixture of 10% H₂/Ar. The H₂ consumption during the process was continuously monitored and quantified using a thermal conductivity detector (TCD).

Electrochemical experiments

The eNO3RR was conducted in a customized H-type cell using a CHI1140C electrochemical workstation. The anodic and cathodic compartments were separated by a Nafion 117 membrane (DuPont). The Nafion 117 membrane was soaked in 5 wt% H₂O₂ solution at 80 °C for 1 h, followed by immersing in deionized water for 30 min. It was then treated with 0.5 M H₂SO₄ at 80 °C for 1 h and rinsed with deionized water for another 30 min before use. The as-synthesized electrocatalyst served as the working electrode. An Ag/AgCl electrode was used as the reference electrode, and a platinum plate was used as the counter electrode. 0.5 M Na₂SO₄ solution (pH = 6.8 ± 0.3) was used as the electrolyte for both the cathode and anode chambers, and 10–140 mM NO₃[−] was added to the cathode chamber. The solution in the cathode chamber was stirred during the process of eNO3RR. All potentials were measured against the Ag/AgCl reference electrode and converted to the reversible hydrogen electrode (RHE) scale using the equation: E(vs. RHE) = E(vs. Ag/AgCl) + 0.1976 V + 0.0591 × pH.

Analytical methods

The concentrations of NH₄⁺, NO₃[−], and NO₂[−] in the electrolyte (diluted to the appropriate concentration) before and after eNO3RR were determined via a colorimetric method.

NH₄⁺ detection: NH₄⁺ was determined by the Nessler's reagent method. 100 μL NaKC₄H₄O₆ solution (500 g/L) and 100 μL Nessler's reagent were added into a 5 mL sample and mixed thoroughly. The absorbance was determined at 420 nm after 20 min.

NO₂[−] detection: 100 μL of color developer (0.04 g of C₁₂H₁₄N₂·2HCl, 0.8 g of sulfonamide, and 2 mL of 85% H₃PO₄ dissolved in 10 mL water) was added to 5 mL of diluted sample, and the reaction was carried out for 10 min at room temperature (20–25 °C). The absorbance was measured at 540 nm.

NO₃[−] detection: 1.1 mL of color developer (1 M HCl and 0.8 wt% NH₂SO₃H) was added to 5 mL of diluted sample. The absorbance was measured at 220 nm and 275 nm after 5 min. The final absorbance value was obtained by the equation of A = A_{220nm} − 2A_{275nm}.

N₂H₄ detection: The color reagent is consisted of 5.99 g of 4-dimethylaminobenzaldehyde (C₉H₁₁NO), 30 mL of concentrated

HCl, and 300 mL of ethanol. The color reagent was added into sample solution (v:v = 1:1), and the mixture was stirred for 10 min at room temperature (20–25 °C). The absorbance was measured at 457 nm. The calibration curve was obtained from N₂H₄ solutions (in 0.1 mol L^{−1} HCl) with known concentrations.

NH₂OH detection: 100 μL of acetate buffer (1.0 M sodium acetate + 1.0 M acetic acid), 100 μL, 4 mM ammonium ferric sulfate solution, and 100 μL, 10 mM 1, 10-phenanthroline ethanolic solution were sequentially added into 3 mL of sample, and the mixture was stood for 20 min at room temperature (20–25 °C). The absorbance was measured at 510 nm.

Isotope labeling experiments

The K¹⁵NO₃ was used as an isotope-labeled N source for eNO3RR. For ¹H NMR (BRUKER AVANCE NEO 600 M) quantification, the pH value of the sample (25 mL) after eNO3RR was adjusted to 2 by adding H₂SO₄. The C₄H₄O₄ (0.01 g) was added as an internal standard. 50 μL of DMSO-d₆ was added into 0.5 mL of the above solution before ¹H NMR test. The calibration curve was obtained using the peak area ratio of ¹⁵NH₄⁺ to C₄H₄O₄ with 50, 100, 150, 200 mg L^{−1} of ¹⁵NH₄⁺ solutions.

Ammonia yield and Faradaic efficiency

FE_{NH₃} was obtained by Eq. (1), and the NH₃ yield was determined via Eq. (2), FE of NO₂[−] was calculated by Eq. (3).

$$FE_{NH_3}(\%) = (8F \times C_{NH_3} \times V) / (M \times Q) \quad (1)$$

$$Yield_{NH_3}(\text{mmol} \cdot \text{h}^{-1} \text{cm}^{-2}) = (C_{NH_3} \times V) / (M \times t \times I) \quad (2)$$

$$FE_{NO_2}(\%) = (2F \times C_{NO_2} \times V) / (46 \times Q) \quad (3)$$

Where *F* is the Faraday constant (96485 C mol^{−1}), *C*_{NH₃} is NH₃ concentration (mol L^{−1}), *V* is the volume of catholyte (L), *Q* is the quantity of charge (C), *M* is the relative molecular mass of NH₃, *t* is the reaction time (s), *I* is the current (A), *C*_{NO₂} is the NO₂[−] concentration (mol L^{−1}).

Density functional theory (DFT) calculation

All the calculations were performed with the projector-augmented plane-wave method implemented in the Vienna ab initio simulation package. The generalized gradient approximation proposed by Perdew-Burke-Ernzerhof (PBE) was selected for the exchange-correlation potential. The cut-off energy for the plane wave was set to 480 eV. The energy criterion was set to 10^{−4} eV in the iterative solution of the Kohn-Sham equation. All the structures were relaxed until the residual forces on the atoms have declined to less than 0.02 eV/Å. To avoid interlaminar interactions, a vacuum spacing of 20 Å is applied perpendicular to the slab. VASPsol code with an implicit solvation model was used to simulate the electrolyte solution to deal with the solvation effect. Here, differences in Gibbs free energy (Δ*G*) (Eq. 4) for intermediates in eNO3RR defined as:

$$\Delta G = \Delta E + \Delta E_{ZPE} - T\Delta S + \Delta G_U \quad (4)$$

where Δ*G* is the total energy difference between the slab and respective terminations computed by DFT-PBE. Δ*E*_{ZPE} and *T*Δ*S* denote differences in zero-point energy and entropy between adsorbed states of reaction intermediates and gap phase, respectively. *T* is the room temperature (20–25 °C). Δ*G*_U = −*eU*, in which *U* is the electrode potential.

Data availability

The data supporting the conclusions of this study are presented in the paper and the supplementary information. Source data are provided in this paper.

References

- Inta, H. R. et al. Recent advances in electrocatalytic NO_x reduction into ammonia. *EES Catal.* **1**, 645–664 (2023).
- Yin, H. et al. Alloying effect-induced electron polarization drives nitrate electroreduction to ammonia. *Chem. Catal.* **1**, 1088–1103 (2021).
- Cheng, X. F. et al. Coordination symmetry breaking of single-atom catalysts for robust and efficient nitrate electroreduction to ammonia. *Adv. Mater.* **34**, 2205767 (2022).
- Fan, Y. et al. Highly efficient metal-free nitrate reduction enabled by electrified membrane filtration. *Nat. Water* **2**, 684–696 (2024).
- Hu, T. et al. Theoretical insights into superior nitrate reduction to ammonia performance of copper catalysts. *ACS Catal.* **11**, 14417–14427 (2021).
- Zhao, R. et al. A Bi-Co corridor construction effectively improving the selectivity of electrocatalytic nitrate reduction toward ammonia by nearly 100%. *Adv. Mater.* **35**, 2306633 (2023).
- Wu, L. et al. Boosting electrocatalytic nitrate-to-ammonia via tuning of N-intermediate adsorption on a Zn-Cu catalyst. *Angew. Chem. Int. Ed.* **62**, e202307952 (2023).
- Yu, J. et al. Boosting electrochemical nitrate-ammonia conversion via organic ligands-tuned proton transfer. *Nano Energy* **103**, 107705 (2022).
- Wei, C. et al. Lattice oxygen-mediated electron tuning promotes electrochemical hydrogenation of acetonitrile on copper catalysts. *Nat. Commun.* **14**, 3847 (2023).
- Li, P. et al. Pulsed nitrate-to-ammonia electroreduction facilitated by tandem catalysis of nitrite intermediates. *J. Am. Chem. Soc.* **145**, 6471–6479 (2023).
- Luo, M. et al. Hydroxide promotes carbon dioxide electroreduction to ethanol on copper via tuning of adsorbed hydrogen. *Nat. Commun.* **10**, 5814 (2019).
- Fan, J. L. et al. Electrochemical reduction of nitrate to ammonia on ultra-stable amorphous Co-P electrocatalyst. *J. Mater. Chem. A* **12**, 20077–20087 (2024).
- Zhang, W. et al. Fluorine modification promoted water dissociation into atomic hydrogen on a copper electrode for efficient neutral nitrate reduction and ammonia recovery. *Environ. Sci. Technol.* **58**, 7208–7216 (2024).
- Wu, Q. et al. Efficient and selective electroreduction of nitrate to ammonia via interfacial engineering of B-doped Cu nanoneedles. *Appl. Catal. B Environ. Energy* **361**, 124597 (2025).
- Yin, H. et al. Electrocatalytic reduction of nitrate to ammonia via a Au/Cu single atom alloy catalyst. *Environ. Sci. Technol.* **57**, 3134–3144 (2023).
- Xie, M. et al. Periodic adjacent Pd-Fe pair sites for enhanced nitrate electroreduction to ammonia via accelerating proton relay. *Adv. Energy Mater.* **14**, 2401717 (2024).
- Fu, W. et al. Tuning mobility of intermediate and electron transfer to enhance electrochemical reduction of nitrate to ammonia on Cu₂O/Cu interface. *Chem. Eng. J.* **433**, 133680 (2022).
- Zhou, J. et al. Achieving efficient and stable electrochemical nitrate removal by in-situ reconstruction of Cu₂O/Cu electroactive nanocatalysts on Cu foam. *Appl. Catal. B Environ. Energy* **317**, 121811 (2022).
- Cheng, D. et al. The nature of active sites for carbon dioxide electroreduction over oxide-derived copper catalysts. *Nat. Commun.* **12**, 395 (2021).
- Wei, Z. et al. Enhancing selective electrochemical CO₂ reduction by in situ constructing tensile-strained Cu catalysts. *ACS Catal.* **13**, 4711–4718 (2023).
- Jansonius, R. P. et al. Strain engineering electrocatalysts for selective CO₂ reduction. *ACS Energy Lett.* **4**, 980–986 (2019).
- Li, C. W. et al. Electroreduction of carbon monoxide to liquid fuel on oxide-derived nanocrystalline copper. *Nature* **508**, 504–507 (2014).
- Kang, W. J. et al. Strain-activated copper catalyst for pH-universal hydrogen evolution reaction. *Adv. Funct. Mater.* **32**, 2112367 (2022).
- Wang, Y. et al. Unveiling the activity origin of a copper-based electrocatalyst for selective nitrate reduction to ammonia. *Angew. Chem. Int. Ed.* **59**, 5350–5354 (2020).
- Xiao, L. et al. Coupling electrocatalytic cathodic nitrate reduction with anodic formaldehyde oxidation at ultra-low potential over Cu₂O. *Energy Environ. Sci.* **16**, 2696–2704 (2023).
- Li, Y. et al. Enhancement of nitrate-to-ammonia on amorphous CeO_x-modified Cu via tuning of active hydrogen supply. *Adv. Energy Mater.* **14**, 2303863 (2024).
- Shi, Y. et al. In-situ reconstructed Cu/Cu₂O heterogeneous nanorods with oxygen vacancies for enhanced electrocatalytic nitrate reduction to ammonia. *Chem. Eng. J.* **479**, 147574 (2024).
- Wei, X. et al. Formic acid electro-synthesis by concurrent cathodic CO₂ reduction and anodic CH₃OH oxidation. *Angew. Chem. Int. Ed.* **60**, 3148–3155 (2021).
- Matte, L. P. et al. Reduction-driven 3D to 2D transformation of Cu nanoparticles. *Small* **18**, 2106583 (2022).
- Dou, Y. et al. Graphene-like holey Co₃O₄ nanosheets as a highly efficient catalyst for oxygen evolution reaction. *Nano Energy* **30**, 267–275 (2016).
- Niveditha, C. V. et al. Comprehensive interfacial study of potential-dynamically synthesized copper oxide thin films for photoelectrochemical applications. *J. Electrochem. Soc.* **163**, H426 (2016).
- Singhal, A. et al. Copper(I) oxide nanocrystals - one step synthesis, characterization, formation mechanism, and photocatalytic properties. *Eur. J. Inorg. Chem.* **2013**, 2640–2651 (2013).
- Eilert, A. et al. Subsurface oxygen in oxide-derived copper electrocatalysts for carbon dioxide reduction. *J. Phys. Chem. Lett.* **8**, 285–290 (2017).
- Tahir, D. et al. Electronic and optical properties of Cu, CuO and Cu₂O studied by electron spectroscopy. *J. Phys: Condens. Matter* **24**, 175002 (2012).
- Sun, W. et al. An efficiently tuned d-orbital occupation of IrO₂ by doping with Cu for enhancing the oxygen evolution reaction activity. *Chem. Sci.* **6**, 4993–4999 (2015).
- Kappen, P. et al. The state of Cu promoter atoms in high-temperature shift catalysts—an in situ fluorescence XAFS study. *J. Catal.* **198**, 56–65 (2001).
- Huang, K. et al. Boosting nitrate to ammonia via the optimization of key intermediate processes by low-coordinated Cu-Cu sites. *Adv. Funct. Mater.* **34**, 2315324 (2024).
- Chen, F. Y. et al. Efficient conversion of low-concentration nitrate sources into ammonia on a Ru-dispersed Cu nanowire electrocatalyst. *Nat. Nanotechnol.* **17**, 759–767 (2022).
- Su, L. et al. Electrochemical nitrate reduction by using a novel Co₃O₄/Ti cathode. *Water Res.* **120**, 1–11 (2017).
- Zheng, W. et al. Self-activated Ni cathode for electrocatalytic nitrate reduction to ammonia: From fundamentals to scale-up for treatment of industrial wastewater. *Environ. Sci. Technol.* **55**, 13231–13243 (2021).
- Chauhan, R. et al. Electrochemical denitrification of highly contaminated actual nitrate wastewater by Ti/RuO₂ anode and iron cathode. *Chem. Eng. J.* **386**, 122065 (2020).
- Fang, J. Y. et al. Copper-based electrocatalysts for nitrate reduction to ammonia. *Materials* **16** (2023).
- Zhang, R. et al. Electrochemical nitrate reduction in acid enables high-efficiency ammonia synthesis and high-voltage pollutants-based fuel cells. *Nat. Commun.* **14**, 8036 (2023).
- Xu, Y. et al. Sulphur-boosted active hydrogen on copper for enhanced electrocatalytic nitrate-to-ammonia selectivity. *Angew. Chem. Int. Ed.* **63**, e202400289 (2024).
- Fan, K. et al. Active hydrogen boosts electrochemical nitrate reduction to ammonia. *Nat. Commun.* **13**, 7958 (2022).

46. Wang, Y. H. et al. In situ Raman spectroscopy reveals the structure and dissociation of interfacial water. *Nature* **600**, 81–85 (2021).
47. Li, C. Y. et al. In situ probing electrified interfacial water structures at atomically flat surfaces. *Nat. Mater.* **18**, 697–701 (2019).
48. Sawata, S. et al. Kinetic evidence based on solvent isotope effects for the nonexistence of a proton-transfer process in reactions catalyzed by a hammerhead ribozyme: Implication to the double-metal-ion mechanism of catalysis. *J. Am. Chem. Soc.* **117**, 2357–2358 (1995).
49. Wang, K. et al. Intentional corrosion-induced reconstruction of defective NiFe layered double hydroxide boosts electrocatalytic nitrate reduction to ammonia. *Nat. Water* **1**, 1068–1078 (2023).
50. Zhang, W. et al. Atypical oxygen-bearing copper boosts ethylene selectivity toward electrocatalytic CO₂ reduction. *J. Am. Chem. Soc.* **142**, 11417–11427 (2020).
51. Zhang, Y. et al. Low-coordinated copper facilitates the *CH₂CO affinity at enhanced rectifying interface of Cu/Cu₂O for efficient CO₂-to-multicarbon alcohols conversion. *Nat. Commun.* **15**, 5172 (2024).

Acknowledgements

This work was supported by the National Natural Science Foundation of China (No. 22222601 and No. 22076019, Y.L.), and the Fundamental Research Funds for the Central Universities (DUT23LAB611, Y.L.).

Author contributions

Q.W. and Y.L. conceived the idea. Q.W., X.F., and Y.L. designed the experiments. Q.W. performed the experiments. L.Q. helped with material characterization. Q.W., X.F., B.S., and X.Q. analyzed the data and discussed the results. Q.W. and Y.L. co-wrote the manuscript. All authors commented on the manuscript. Y.L. supervised the whole project.

Competing interests

The authors declare no competing interests.

Additional information

Supplementary information The online version contains supplementary material available at <https://doi.org/10.1038/s41467-025-58811-5>.

Correspondence and requests for materials should be addressed to Yanming Liu.

Peer review information *Nature Communications* thanks Chun-Chih Chang, Zhihui Ai, and the other anonymous reviewer(s) for their contribution to the peer review of this work. A peer review file is available.

Reprints and permissions information is available at <http://www.nature.com/reprints>

Publisher's note Springer Nature remains neutral with regard to jurisdictional claims in published maps and institutional affiliations.

Open Access This article is licensed under a Creative Commons Attribution-NonCommercial-NoDerivatives 4.0 International License, which permits any non-commercial use, sharing, distribution and reproduction in any medium or format, as long as you give appropriate credit to the original author(s) and the source, provide a link to the Creative Commons licence, and indicate if you modified the licensed material. You do not have permission under this licence to share adapted material derived from this article or parts of it. The images or other third party material in this article are included in the article's Creative Commons licence, unless indicated otherwise in a credit line to the material. If material is not included in the article's Creative Commons licence and your intended use is not permitted by statutory regulation or exceeds the permitted use, you will need to obtain permission directly from the copyright holder. To view a copy of this licence, visit <http://creativecommons.org/licenses/by-nc-nd/4.0/>.

© The Author(s) 2025